Inorganic Chemistry

pubs.acs.org/IC

Article

Tuning the Structural and Magnetic Properties in Mixed Cation $Mn_xCo_{2-x}P_2S_6$

Matthew Cheng,○ Abishek K. Iyer,○ Xiuquan Zhou, Alexander Tyner, Yukun Liu, M. Arslan Shehzad, Pallab Goswami, Duck Young Chung, Mercouri G. Kanatzidis,* and Vinayak P. Dravid*

Cite This: Inorg. Chem. 2022, 61, 13719−13727

Read Online

ACCESS | Metrics & More | Article Recommendations | Supporting Information

ABSTRACT: The metal thiophosphates (MTP), $M_2P_2S_6$, are a versatile class of van der Waals materials, which are notable for the possibility of tuning their magnetic properties with the incorporation of different transition-metal cations. Further, they also offer opportunities to probe the independent and synergistic role of the magnetically active cation sublattice when coupled to P_2Q_6 polyhedra. Herein, we report the structural, magnetic, and electronic properties of the series of MTPs, $Mn_xCo_{2-x}P_2S_6$ (x = 0.25, 0.5, 1, 1.5, 1.75) synthesized by the P_2S_5 flux method. Structural and elemental analysis indicates a homogeneous stoichiometry in the $Mn_xCo_{2-x}P_2S_6$ compounds. We observe that a correlation is apparent between the intensities of specific Raman modes and Raman shifts with respect to the alloying ratio between Mn and Co. Magnetic susceptibility measurements indicate that the alloyed systems adopt an ordered antiferromagnetic (AFM) configuration with a dependence of the Néel temperature on the alloying ratio. A possible magnetic frustration behavior was observed for the composition $MnCoP_2S_6$ due to magnetic moment compensation as the alloying ratio between Mn and Co approaches parity. Interestingly, mixed oxidation states of the metal cation species are also observed in $Mn_xCo_{2-x}P_2S_6$ along with a linear dependence of the work function on the alloying ratio of Mn and Co.

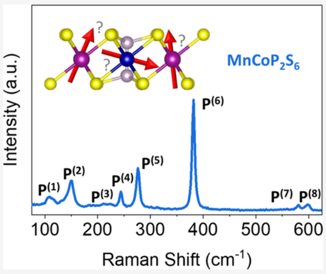

1.0. INTRODUCTION

The transition-metal chalcophosphates (MCPs, $MM'P_2Q_6$) are layered systems characterized by ethane-like $[P_2Q_6]^{4-}$ anions where each phosphorus atom is coordinated by three chalcogen atoms in a honeycomb lattice with metal cations occupying 2/3 of the octahedral sites within the lattice.[1,2] Unlike other layered systems such as MoQ_2, these compounds can incorporate a much higher degree of metal substitution as long as the M and M' valency adds to 4+. Thus, M and M' can both have a charge of 2+ resulting in an alloy such as $MnFeP_2S_6$, or M = 1 + and M' = 3 + resulting in an alloy such as $LiInP_2Se_6$.[3,4] The MCPs have garnered significant interest for their tunable optical, electronic, and magnetic properties and have been studied extensively for applications in catalysis, cathode materials in lithium batteries, and nanoelectronics.[5−7] Particular attention has been paid to the magnetic properties of the metal thiophosphates (MTPs, $M_2P_2S_6$), and extensive studies have been conducted by incorporating magnetic cations such as Mn, Fe, Co, and Ni into the $[P_2S_6]^{4-}$ lattice.[8−11] In the bulk, all of these previously reported monometallic MTPs have long-range antiferromagnetic (AFM) order but with very different magnetic anisotropy that is determined by the transition metal M and the layered nature of the MTPs.[10−13] For example, the magnetic moments of $Fe_2P_2S_6$ and $Mn_2P_2S_6$ align predominantly perpendicular to the basal plane, while the magnetic moments of both $Ni_2P_2S_6$ and $Co_2P_2S_6$ align parallel to the basal plane.[10,12] More specifically, $Co_2P_2S_6$ and $Ni_2P_2S_6$ are anisotropic Heisenberg AFM systems with magnetic moments aligning along the basal plane, predominantly along the a-axis.[10,11] While $Fe_2P_2S_6$ is a strongly anisotropic Ising AFM system with all of its magnetic moments aligning parallel to the out-of-plane direction (c^*-axis), $Mn_2P_2S_6$ is a weakly anisotropic Heisenberg AFM system with its magnetic moments aligning almost parallel to the c^*-axis with a small in-plane component.[12,14]

Given the capability of $M_2P_2S_6$ systems to incorporate these different transition metals that directly impact the anisotropy of the magnetism there is an interest in tuning this property by chemical substitution. Comprehensive studies have been conducted on $Mn_{2-x}Fe_xP_2S_6$, where the magnetic moments of both monometallic $Mn_2P_2S_6$ and $Fe_2P_2S_6$ align perpendicular to the basal plane, while in $Mn_{2-x}Ni_xP_2S_6$, the magnetic moments of Ni are aligned parallel to the basal plane.[15,16] A significant impact on the magnetic susceptibility is observed as a function of the alloying ratio between the metal cations in each case. The effect of the alloying on the associated long-range ordering temperatures, $T_{Néel}$, for some of these previously reported mixed MTPs are shown in Table S1.[3,15,17,18] However, there is a distinct lack of comprehensive

Received: April 2, 2022
Published: August 23, 2022

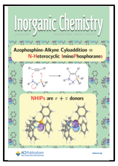

structural and magnetic studies including Co in mixed MTPs. This is due to the challenging synthesis of Co-based MTPs due to the formation of the parasitic phase of CoP_xS_{2-x}.[19] Chica et al. have previously reported a rapid synthesis method using a P_2S_5 flux and studied the formation of supposedly phase-pure $Co_2P_2S_6$ as determined by pXRD.[19] This opened up the way to discover new bimetallic thiophosphates, which can incorporate Co, $FeCoP_2S_6$, and $MnCoP_2S_6$.[19]

Motivated by these results, the P_2S_5 flux is utilized to synthesize new Co-based bimetallic MTPs. In this article, we report on the synthesis and characterization of a series of $Mn_xCo_{2-x}P_2S_6$. Taking a top-down approach, pXRD and other spectroscopic techniques including Raman spectroscopy, scanning transmission electron microscopy energy-dispersive spectroscopy (STEM-EDS), X-ray photoelectron spectroscopy (XPS), and ultraviolet photoelectron spectroscopy (UPS) are used to investigate the crystal structure of solid solutions of $Mn_xCo_{2-x}P_2S_6$. From the Raman spectroscopy, specific phonon mode shifts and relative peak intensity variations that depend on the alloying ratio of Mn/Co are observed in a similar manner to a previous study on $Fe_{2-x}Co_xP_2S_6$.[20] STEM-EDS measurements of the alloyed samples indicate a homogeneous distribution of both Mn and Co in all samples analyzed. Magnetic susceptibility measurements were also performed on powdered samples of $Mn_xCo_{2-x}P_2S_6$. The two most significant observations from these susceptibility measurements are the significant shift in the long-range ordering temperature, $T_{\text{Néel}}$, as a dependence on the ratio of Mn/Co and the possible discovery of impurity phases of CoP_xS_{2-x} in the end member, $Co_2P_2S_6$, that was not detected by the other characterization methods. This emphasizes the difficulties in synthesizing phase-pure Co-containing thiophosphate systems, and further study is necessary.

2.0. EXPERIMENTAL METHODS

2.1. Synthesis of $Mn_xCo_{2-x}P_2S_6$.

Chemical reagents: The following reagents were used as they were received: manganese powder (99.9%, Cerac), cobalt powder (99.8%, Cerac), and phosphorus pentasulfide powder (99%, Sigma-Aldrich). The solvents used were house-deionized (DI) water, anhydrous ethanol (Fisher Chemical), and acetone (Fisher Chemical, 99.5%).

The compounds were synthesized using the reactive P_2S_5 flux method, which is described in the paper by Chica et al.[19] The M (M/M') to P_2S_5 ratio was 2:3 and 1:1:3 for the monometallic and bimetallic thiophosphates, respectively. In a nitrogen-filled glovebox, metal and P_2S_5 powders were loaded into 12.7 mm OD and 10.5 mm ID fused silica tubes with a total charge mass of 2 g. The amounts used are tabulated in Table S2. The tubes were sealed with an oxy/natural gas torch under the pressure of ~3×10^{-3} mbar. After sealing, the tubes were mechanically agitated for 10 min to ensure mixing of the reagents. The tubes were processed using a computer-controlled tube furnace and the following heating profile was followed: heating from room temperature to 540 °C in 10 h, annealing for 72 h at 540 °C, cooling to 250 °C in 12 h, and then the furnace was turned off to continue cooling to room temperature. Warning: The removal of the flux must be performed in a fume hood as this reaction releases H_2S gas. In a fume hood, the silica ampoule was opened and the ingot was placed in a 20 mL scintillation vial with 10 mL of a 50/50 vol/vol mixture of DI water and ethanol (50/50 H_2O/EtOH) and heated to ~70 °C for 1 h. If any flux remained, the solution was decanted and 10 mL of 50/50 H_2O/EtOH was added and heated for 1 h. After the removal of the flux, the product was washed twice with DI water and twice with acetone. The residual thiols were left to off-gas overnight. The composition of all of the compounds was confirmed using STEM-EDS (Table S3).

2.2. Magnetic Susceptibility Measurements.

Magnetic susceptibility measurements were carried out using a magnetic property measurement system (Quantum Design MPMS). Both field-cooled (FC) and zero-field-cooled (ZFC) magnetic susceptibility measurements were made from 1.8 to 300 K with an applied magnetic field of 1000 Oe. Curie–Weiss fits were conducted on the linear region (>200 K to room temperature) of the inverse magnetic susceptibility plots to determine the slope, C, and the Curie–Weiss temperature, Θ. The effective magnetic moment μ_{eff} is calculated from this slope, where $\mu_{\text{eff}} = \sqrt{8^*C}$.

2.3. X-ray Photoelectron Spectroscopy (XPS) and Ultraviolet Photoelectron Spectroscopy (UPS).

The samples were crushed in a mortar and pestle and then sonicated in ethanol. Next, the samples were drop-cast on silicon wafers with 300 nm of SiO_2 thermal oxide until a dense and uniform layer is formed. Room-temperature XPS spectra were collected with Thermo Scientific ESCALAB 250Xi. A 500 μm spot size from a monochromatic Al Kα source was used, and the chamber pressure was kept at 1.5×10^{-8} mbar during analysis. All spectra were calibrated relative to the carbon peak at 284.8 eV. The background subtraction was done using the Shirley method. Thermo Scientific ESCALAB 250Xi was also used for UPS studies. The gas discharge lamp is employed with admitted He gas (He I (21.2 eV) emission line). During UPS analysis, the pressure inside the chamber was kept constant at 3×10^{-8} mbar.

2.4. DFT Simulations of Raman modes.

All first-principles calculations are based on density functional theory and were performed using the Quantum ESPRESSO software package.[21,22] The calculations utilize the generalized gradient approximations (GGA) of Perdew–Burke–Ernzerhof (PBE).[23] To account for the interlayer van der Waals forces, we implement the semiempirical DFT-D2 of Grimme.[24] A plane-wave cutoff of 80 Ry is used in all calculations. For bulk calculations, the primitive unit cell is sampled with a k-mesh of 6 × 3 × 5. The lattice parameters and atomic positions are given by Ouvrard et al.;[25] however, the atomic positions are relaxed before proceeding with calculation of the phonon modes.

3.0. RESULTS AND DISCUSSION

A top-down approach is undertaken with the analysis of $Mn_xCo_{2-x}P_2S_6$, and the results are presented as follows. First, powder X-ray diffraction (pXRD) is used to confirm the crystal structure of the solid solutions of $Mn_xCo_{2-x}P_2S_6$ in the bulk and is corroborated at the nanoscale with scanning transmission electron microscopy (STEM). Next, Raman spectroscopy is presented. A distinct correlation between the alloying ratio of Mn to Co and specific features of each recorded spectra is observed. This is followed by an analysis of the magnetic susceptibility of these systems. A distinct antiferromagnetic behavior is observed in all alloyed $Mn_xCo_{2-x}P_2S_6$ as well as parasitic ferromagnetism due to trace impurities at low temperatures. Finally, the oxidation states of the ion species and the electronic structure of $Mn_xCo_{2-x}P_2S_6$ are evaluated with X-ray photoelectron spectroscopy (XPS) and ultraviolet photoelectron spectroscopy (UPS).

3.1. Powder X-ray Diffraction (PXRD).

Previous reports on both $Mn_2P_2S_6$ and $Co_2P_2S_6$ indicate both systems crystallize in the space group $C2/m$. As has been discussed in other articles,[19,26] the metal cations are encapsulated in a cage of $[P_2S_6]^{4-}$ anions.[1,2] Figure 1a shows the crystal structure of the monometallic systems consists of 2/3 of the octahedral sites occupied by either Mn^{2+} or Co^{2+} cations with 1/3 of the sites occupied by a phosphorus dimer. In this study, we focused on the solid solubility of Mn in $Co_2P_2S_6$. PXRD confirms that $Mn_xCo_{2-x}P_2S_6$ (x = 0.25 to 1.75) crystallizes into the monoclinic space group $C2/m$. These solid solutions were successfully obtained by annealing the compounds at 540 °C

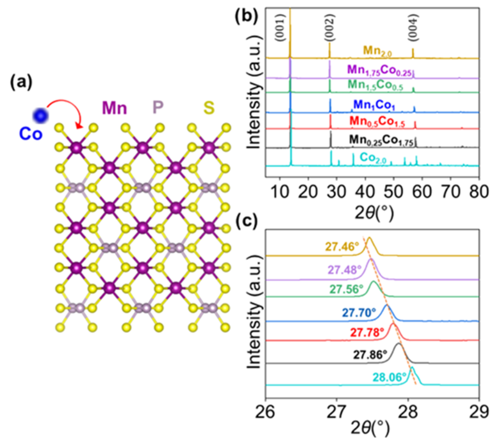

Figure 1. (a) Schematic of $Mn_xCo_{2-x}P_2S_6$ crystal structure. (b) Powder X-ray diffraction (PXRD) of alloyed $Mn_xCo_{2-x}P_2S_6$ with emphasized peaks corresponding to (00*l*)-planes. (c) Inset of pXRD peak exhibiting distinct linear shifts to lower 2θ as a result of the incorporation of greater concentration of Mn in $Mn_xCo_{2-x}P_2S_6$ in accordance with Vegard's Law.

for 72 h. This temperature profile was changed to 540 from 580 °C as reported by Chica et al,[19] since in the Co-rich phases, small amounts of CoP_xS_{2-x} were observed. At 540 °C, we observed no impurity of the CoP_xS_{2-x} phase in the pXRD. Attempts to grow large single crystals by increasing the annealing times up to 72 h did not result in a significant increase in crystal size.

Structural analysis of the phase purity of these solid solutions has been carried out with pXRD (see SI Section 2.0). The most distinct peaks correspond to the (00*l*) planes for all alloyed $Mn_xCo_{2-x}P_2S_6$ (x = 0, 0.25, 0.5, 1, 1.5, 1.75, 2.0) as shown in Figure 1b. The diffraction pattern for each alloyed system is normalized with respect to the (001) peak, the tallest peak in all 7 diffractograms. With increasing amounts of Mn introduced relative to Co, a distinct shift to lower 2θ is observed. To emphasize this behavior, the (002) peak for the 7 alloyed systems is shown in Figure 1c. A linear shift to lower 2θ is clearly observed with increasing Mn concentration for (002). The expected 2θ for the (002) peak for $Mn_2P_2S_6$ and $Co_2P_2S_6$ are 27.5 and 28.0°, respectively.[2] The measured 2θ for the (002) peak for $Mn_2P_2S_6$ and $Co_2P_2S_6$ are 27.5 and 28.1°, respectively. These values are fairly close to the expected values and indicate this system's adherence to Vegard's law. The experimentally measured lattice parameters for $Mn_2P_2S_6$($Co_2P_2S_6$) are a = 6.07 Å(5.90 Å), b = 10.52 Å (10.22 Å), c = 6.79 Å (6.66 Å) and β =107.35°(107.17°). The obtained cell constants from powder XRD refinements can be seen in Table 1. The refinements suggest a gradual increase in volume with an increasing concentration of Mn. Furthermore, the Rietveld refinements of select $Mn_xCo_{2-x}P_2S_6$ indicate nearly all samples are homogeneous solid solutions in the bulk. However, there may be some P_xS_y poly-chalcogenide impurity phase present in the bulk $MnCoP_2S_6$ diffraction pattern that is likely a result of the P_2S_5 flux and indicates that there may be some variation in the presence of flux residue even after the washing procedure even if the predominant product is the desired $Mn_xCo_{2-x}P_2S_6$ system (Figure S2). It is noted that there is some variation in the relative intensity of peaks, but this is due to variations in the orientation of different powdered samples during measurement. The peaks corresponding to the (00*l*) planes are still the most intense peaks as they are the preferred orientation of these layered van der Waals materials when crushed to powder to conduct PXRD measurements.

3.2. High-Resolution Transmission Electron Microscopy (HRTEM) and Scanning Tunneling Electron Microscopy with Energy-Dispersive Spectroscopy (S/TEM-EDS). To further understand the structure and chemical homogeneity of the alloyed system at different length scales, scanning/transmission electron microscopy (S/TEM) analysis (see Methods in SI Section 3.0) is conducted on exfoliated $Mn_xCo_{2-x}P_2S_6$ (x = 0.25, 0.5, 1, 1.5, 1.75). Figure 2a presents a representative bright-field TEM image of an $Mn_{0.5}Co_{1.5}P_2S_6$ flake, while an HRTEM image of the highlighted region along the [103] zone axis (c*-axis) is shown in Figure 2b with its

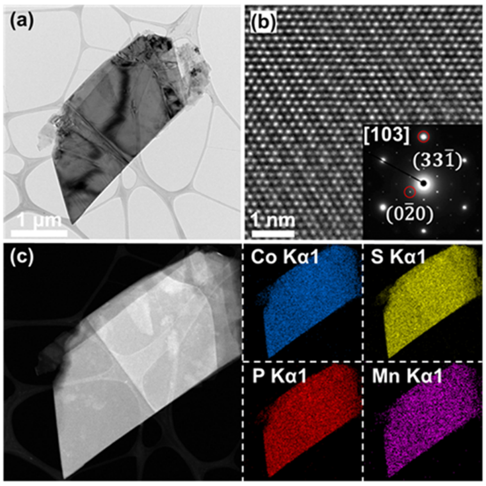

Figure 2. (a) Representative bright-field TEM image of $Mn_{0.5}Co_{1.5}P_2S_6$ exhibiting distinct layered structure with notable terracing that occurs during exfoliation. (b) HRTEM image of $Mn_{0.5}Co_{1.5}P_2S_6$ with inset diffraction pattern along [103]-axis (c*-axis). (c) HAADF-STEM image of same flake with accompanying EDS maps indicating the homogeneous distribution of Mn, Co, P, and S at the given length scales.

Table 1. Cell Constants Obtained from Powder Refinement of $Mn_xCo_{2-x}P_2S_6$ (x = 0−2)

compound	a (Å)	b (Å)	c (Å)	β	V (Å^3)
$Mn_2P_2S_6$	6.083 (3)	10.534 (2)	6.801 (2)	107.461 (7)	415.74 (9)
$Mn_{1.75}Co_{0.25}P_2S_6$	6.0834 (3)	10.534 (2)	6.8011 (2)	107.461 (7)	415.74 (2)
$Mn_{1.5}Co_{0.5}P_2S_6$	6.0200 (2)	10.4621 (2)	6.761 (1)	107.229 (2)	406.70 (1)
$MnCoP_2S_6$	5.9910 (2)	10.3720 (2)	6.7372 (1)	107.090 (6)	399.98 (3)
$Mn_{0.5}Co_{1.5}P_2S_6$	5.9327 (4)	10.2922 (3)	6.692 (2)	107.110 (9)	390.38 (5)
$Mn_{0.25}Co_{1.75}P_2S_6$	5.9032 (3)	10.2192 (6)	6.6692 (1)	107.217 (3)	384.21 (4)
$Co_2P_2S_6$	5.906 (14)	10.2192 (6)	6.668 (16)	107.217 (5)	384.21(2)

selected area diffraction pattern (SAED) as the inset. The HRTEM image and SAED pattern reveal the single-crystalline nature of the flake. The observed sixfold rotational symmetry in the SAED pattern is due to the presence of 120° rotational twin boundaries, which has been previously reported by Cheng et al. in $Fe_xCo_{2-x}P_2S_6$ and Murayama et al. in $Fe_2P_2S_6$.[27] Diffraction patterns of $Mn_2P_2S_6$ and $Co_2P_2S_6$ are simulated using SingleCrystal[28] to better illustrate this phenomenon; 120° (blue) and 240° (red) rotations of the diffraction pattern are overlapped with the unrotated pattern (black) to represent impact from the 120° rotational twin boundaries (Figure S4a); the simulation result is consistent with the observed SAED patterns with the consideration that the different cation sizes of Mn and Co lead to different lattice parameters and the resulting positions of diffraction spots. Figure 2c is the STEM High-angle annular dark field (HAADF) image of the same flake with the energy-dispersive spectrum (EDS) map for Co, Mn, P, and S. The uniform distribution of the colors in the map indicates the chemical homogeneity of the synthesized compound and confirms that no secondary phases are formed in the observed crystals at the given length scale. EDS maps for the other alloyed $Mn_xCo_{2-x}P_2S_6$ (x = 0.25, 1, 1.5, 1.75) systems in Figure S5 indicate a similar homogeneous distribution of Mn, Co, P, and S at the given length scales. Elemental compositions for nominally stoichiometric $Mn_xCo_{2-x}P_2S_6$ (x = 0.25, 0.5, 1, 1.5, 1.75) are evaluated and shown in Table S3 with accompanying EDS spectra in Figure S6. It is observed that all alloyed systems are of expected composition. The HRTEM and EDS analysis results support that $Mn_xCo_{2-x}P_2S_6$ (x = 0.25, 0.5, 1, 1.5, 1.75) can be synthesized with high crystallinity and chemical homogeneity using the P_2S_5 flux method.

3.3. Raman Spectroscopy. The structural changes that are observed due to alloying of Mn and Co in $Mn_xCo_{2-x}P_2S_6$ will alter the phonon contributions within the lattice. Therefore, Raman spectroscopy plays a crucial role in analyzing these atomic vibrations and is also a facile method to confirm the alloying ratio of cation species within the $[P_2S_6]^{4-}$ anion lattice. Previous reports on MPS_3 phases with C_{2h} symmetry exhibit eight Raman peaks.[29−36] However, there has been some confusion in previous studies on assigning phonon modes of these specific peaks in bulk samples.[32−34] In the bulk, the MPS_3 systems have C_{2h} symmetry with Raman modes described by 8 A_g modes ad 7 B_g modes.[29,30] However, the $[P_2S_6]^{4-}$ anion unit, which describes the symmetry of a monolayer of the MPS_3 phase, has D_{3d} symmetry and is described with 3 A_{1g} modes and 5 E_g modes.[34,35] However, as discussed by Sun et al., the A_g modes associated with the C_{2h} symmetry group have the same symmetry properties as the A_{1g} modes in the D_{3d} symmetry group and the pairs of A_g and B_g modes in the C_{2h} group have similar symmetry properties to that of E_g in the D_{3d} group.[30] In the context of this study, which is on bulk samples, the associated Raman modes will be considered with the C_{2h} symmetry group.

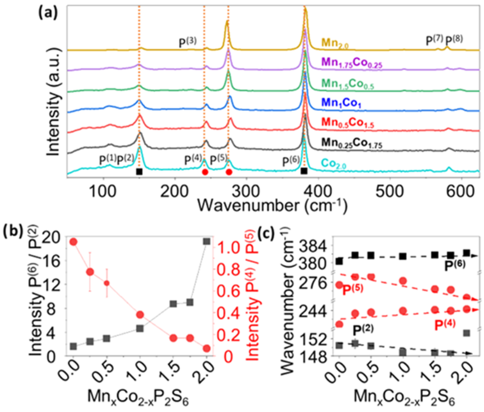

Figure 3. (a) Normalized Raman spectra for all alloyed $Mn_xCo_xP_2S_6$ alloys systems with $Mn_2P_2S_6$ reference. Peaks are labeled with the $P^{(x)}$ notation to indicate the presence of a peak. $P^{(1)}$, $P^{(2)}$, $P^{(3)}$, $P^{(5)}$, and $P^{(7)}$ correspond to Ag, Bg modes. While $P^{(4)}$, $P^{(6)}$, and $P^{(8)}$ correspond to solely A_g modes. Orange lines are drawn through the four most unambiguous peaks and labeled with a black square or red circle, respectively. (b) Intensity ratio of $P^{(6)}/P^{(2)}$ and $P^{(4)}/P^{(5)}$ as a function of the alloying ratio between Co and Mn. (c) Raman blueshifts and redshifts of peaks at wavenumbers ~152, ~244, ~276, and ~384 cm^{-1}. Peaks composed solely of A_g modes blue-shift, while modes composed of A_g, B_g modes red-shift as the ratio of Mn:Co increases.

The observed Raman modes are attributed to the vibration of the P and S anion cage relative to the cation species and all changes will be observed in changes in the Raman spectra features (see Methods in SI Section 4.0). Peaks at wavenumbers below 150 cm^{-1} are associated with cation vibrations while modes above this wavenumber cutoff are dominated by the P−P dimer or $[P_2S_6]^{4-}$ anion units.[31,32,34,35] Figure 3a shows normalized Raman spectra of bulk samples for $Mn_xCo_{2-x}P_2S_6$ from 50 to 650 cm^{-1}. The reference Raman spectra for $Co_2P_2S_6$ and $Mn_2P_2S_6$ matches well with reported values[31,34] and its synthesis process is detailed in an earlier publication by Chica et al.[19] A notable change in the ratio of two pairs of the most unambiguous peaks is observed at: $P^{(4)}(A_g)$ mode ~245 cm^{-1} and $P^{(5)}(A_g, B_g)$ mode at ~272 cm^{-1} and at $P^{(6)}(A_g)$ mode ~380 $cm^{-1}$and $P^{(2)}(A_g, B_g)$ mode ~150 cm^{-1}. As we have previously reported in the $Fe_{2-x}Co_xP_2S_6$ system[20] the variation in the intensity of these two pairs of peaks is strongly correlated with the alloying ratio between the cation species as is shown in Figure 3b. In a similar trend with the $Fe_{2-x}Co_xP_2S_6$ system, as the Co content of the sample is reduced the intensity ratio $P^{(4)}/P^{(5)}$ is also reduced while the intensity ratio $P^{(6)}/P^{(2)}$ is increased in a linear manner. This relationship between the intensity ratios of these specific Raman modes can be used to identify specific alloying ratios in the thiophosphate systems.

Furthermore, a distinct shift of the wavenumber is observed for these four prominent Raman modes that is dependent on the alloying ratio as well. A redshift is observed for $P^{(2)}(A_g, B_g)$ and $P^{(5)}(A_g, B_g)$ while a blueshift is observed for $P^{(4)}(A_g)$ and $P^{(6)}(A_g)$ with increasing concentration of Mn as presented in Figure 3c. However, it is observed that an exception to this trend is apparent for $P^{(2)}(A_g, E_g)$ in $Mn_2P_2S_6$ where a distinct shift to a higher wavenumber is observed. The effect of alloying on the wavenumber shift of Raman modes has been previously reported in alloyed $Mo_{1-x}W_xS_2$.[37,38] Chen et al. have observed a distinct blueshift for the out-of-plane A_1' mode, a blueshift in the in-plane WS_2-like E′ mode, and a redshift in the in-plane MoS_2-like E′ mode as the W content is increased.[37] As there is a separation of approximately 25 cm^{-1} between these two E′ modes, it is straightforward to identify each peak and observe the blueshifts and redshifts as the alloying ratio between Mo and W is varied. In the case of $Co_2P_2S_6$ and $Mn_2P_2S_6$, the four most prominent peaks of interest are separated by, at most, 6 cm^{-1}.[30,32] Thus, when Mn and Co are alloyed together in $Mn_xCo_{2-x}P_2S_6$, it becomes much more difficult to deconvolute the contributions from $Mn_2P_2S_6$-like A_g and B_g modes and

https://doi.org/10.1021/acs.inorgchem.2c01116
Inorg. Chem. 2022, 61, 13719−13727

$Co_2P_2S_6$-like A_g and B_g modes, as it is expected that there will be redshifts and blueshifts for each respective mode.

To gain greater insight into the contributions of the metal cations and the $[P_2S_6]^{4-}$ anion unit, first-principles DFT calculations were conducted on the bulk layered system of $Mn_2P_2S_6$. As previously stated, many theoretical studies on $Mn_2P_2S_6$ have considered the layers as decoupled.[35,36] While the full-layered system supports C_{2h} symmetry, if we consider only a single layer, the symmetry is raised to D_{3d}.[36] To replicate the system as genuinely as possible, we consider the full-layered system in our simulation. As such, we find no E_g modes, only A_g and B_g modes. The resulting modes at the γ location are shown in Figure S7. Karagar et al. have reported on phonon dispersion simulations on $Fe_2P_2S_6$ and the resulting modes are comparable.[29] The four most prominent peaks of interest are at ∼153, ∼244, ∼273, and 382 cm^{-1}. If we are to consider the peak ∼153 cm^{-1} as A_g, B_g, it is close to the average of the two nearby simulated peaks, 144.4 cm^{-1} (B_g) and 170.3 cm^{-1} (A_g). Next, if we are to consider the peak ∼244 cm^{-1} as A_g, the two closest simulated modes are at 244.1 cm^{-1} (B_g) and 249.8 cm^{-1} (A_g), which indicates the limitation of the accuracy of our simulated model, which is not unexpected for modes to be off expected values by up to 10 cm^{-1}. Third, the peak near ∼273 cm^{-1} is expected to be A_g, B_g and has two closest simulated peaks at 271.8 cm^{-1} (A_g) and 273.1 cm^{-1} (B_g). Finally, the peak close to 382 cm^{-1}, which is expected to be an A_g mode, does indeed have a simulated mode nearby at 387.3 cm^{-1}. However, further investigations will be necessary to quantify the contributions of the $Co_2P_2S_6$-like and $Mn_2P_2S_6$-like Raman modes. Nevertheless, these alloying-based Raman shifts are also useful in identifying and quantifying the Mn/Co ratio in the mixed metal $Mn_xCo_{2-x}P_2S_6$ system.

3.4. Magnetic Susceptibility Measurements. Figure 4 shows the magnetic behavior as a function of temperature for the alloyed $Mn_xCo_{2-x}P_2S_6$ system with $Mn_2P_2S_6$ included as a reference. All measurements are conducted with a magnetic field of 1000 Oe. Nearly all of the alloyed $Mn_xCo_{2-x}P_2S_6$ systems exhibit an overall similar behavior with the exception of $MnCoP_2S_6$ where the Mn:Co ratio is 1:1. The first feature of note is a broad maximum temperature, T_{Max}, which is attributed to low-dimensional spin correlations in these layered chalcogen systems.[11,12,16] The second feature of note is an inflection point at a lower temperature, $T_{Néel}$, that indicates a phase transition to a long-range antiferromagnetic state.[12,16] The Néel temperature, $T_{Néel}$, is defined as the peak in the derivative of the magnetic susceptibility with respect to temperature, $d\chi/dT$ (Figure S8).[12,16] Figure 4 shows both the T_{Max} and $T_{Néel}$ for all of the alloyed samples and $Mn_2P_2S_6$. It is of interest to note that both the T_{Max} and $T_{Néel}$ of $Mn_2P_2S_6$ are in accordance with previously reported values.[12,16,39] With the introduction of Co into the alloyed system, T_{Max} and $T_{Néel}$ decrease until $Mn_{1.5}Co_{0.5}P_2S_6$ where a minimum $T_{Néel}$ = 36 K is reached before increasing with further Co alloying. This is compared to other previously reported $M_xM'_{2-x}P_2S_6$ (Table S1) such $Mn_{2-x}Fe_xP_2S_6$ and $Mn_{2-x}Ni_xP_2S_6$, where a minimum $T_{Néel}$ is reached with a greater degree of alloying at x = ∼1.0. It must be stated that in these previous studies, the composition at x = 1.0 does have a broad maximum at T_{Max}, while in $MnCoP_2S_6$, the broad maximum at T_{Max} is completely suppressed. This will likely have an impact on the determined $T_{Néel}$ of $MnCoP_2S_6$. Bai et al. have previously observed the suppression of the broad maximum in exfoliated $Mn_2P_2S_6$ and attributed this behavior to the spins on Mn^{2+} aligning off antiparallel to one another and forming a perturbation state with a net nonzero magnetization and a weak ferromagnetic interaction.[39] In the case of $MnCoP_2S_6$, it may be the case that a similar perturbation state is induced in the bulk through alloying with Co but further measurements and analysis must be done. Another feature of note is the rapid rise in the magnetic susceptibility at a temperature below $T_{Néel}$ at $T < 30$ K in all of the alloyed systems which is a likely indication of parasitic ferromagnetism. In previous magnetic susceptibility studies of metal thiophosphate systems, authors have attributed this increase in the magnetic susceptibility to the presence of minor impurities present in the sample.[10,34] From M vs H measurements at 2 and 150 K for $MnCoP_2S_6$, it can be seen that when above the ordering temperature, the M vs H behavior is linear, while below 2 K, the M vs H behavior is S-shaped and is indicative of weak ferromagnetism (Figure S9). Thus, this increase in the magnetic susceptibility may likely be due to the presence of trace ferromagnetic impurities, which may have formed through the presence of P_xS_y residue from the flux as discussed in Section 3.1.

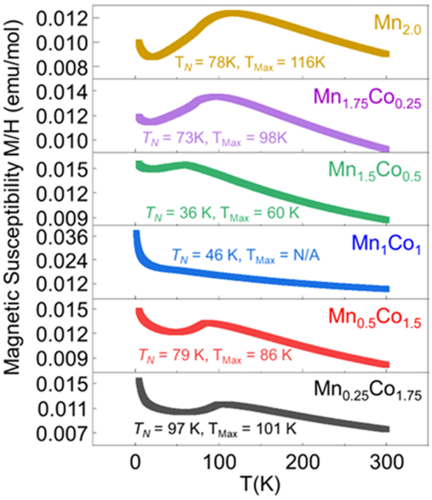

Figure 4. Field-cooled (FC) magnetic susceptibility curves of alloyed systems of $Mn_xCo_{2-x}P_2S_6$ with H = 1000 Oe. In all magnetic susceptibility curves, the characteristic transition from the paramagnetic regime to antiferromagnetic regime is observed. The expected reduction in the Néel temperature as Mn and Co approaches parity with one another is also observed.

A final observation of note is in the difference of the $Co_2P_2S_6$ magnetic susceptibility behavior from previous reports (Figure S8).[10,34] $Co_2P_2S_6$ should exhibit a broad maximum and $T_{Néel}$ indicated by the sharp peak in the plot of $d\chi/dT$, both of which are not present (Figure S8). The magnetic susceptibility is also observed to rapidly increase as a function of temperature as the temperature is lowered to 2 K. The rapid increase in the susceptibility is indicative of a weak ferromagnetism. Furthermore, the magnetic susceptibility is an order of magnitude higher than the other measured samples. A possible explanation for this is the formation of the impurity phase CoP_xS_{2-x}, which exhibits ferromagnetic behavior.[40] This is intriguing as this impurity phase was not observed through the bulk structural characterization by PXRD (Figure S2c) or Raman. This highlights the difficulty in stabilizing phase-pure $Co_2P_2S_6$.

https://doi.org/10.1021/acs.inorgchem.2c01116
Inorg. Chem. 2022, 61, 13719−13727

To further evaluate the impact of alloying on the magnetic susceptibility of the alloyed $Mn_xCo_{2-x}P_2S_6$, the field-cooled (FC) and zero-field-cooled (ZFC) susceptibility measurements are compared (Figure S10). In all alloyed $Mn_xCo_{2-x}P_2S_6$, no significant difference between the ZFC and FC is observed at any temperature. This indicates that spin glass-like behavior is unlikely to occur in $Mn_xCo_{2-x}P_2S_6$ at any composition. To give perspective, it has been previously reported by Rao et al. that $Fe_{2-x}Ni_xP_2S_6$ behaves in a similar manner where there is no difference between the FC and ZFC magnetic susceptibility curves below the ordering temperature.[13] In contrast, Masubuchi et al. have reported that spin frustration is apparent in specific compositions of $Mn_{2-x}Fe_xP_2S_6$, where there is a distinct deviation between the FC and ZFC curves below the order temperature.[15] The extent of this frustration is evaluated with the frustration parameter, defined as $f = |\Theta_{CW}|/T_N$, as reported by Balent (Table S4).[41] The Curie−Weiss constant, Θ_{CW}, is determined by fitting the linear paramagnetic region of the inverse susceptibility curves at $T > 200$ K (Figure S11). According to Balent, a frustration parameter, f, that is greater than 5−10 indicates a strong suppression of ordering due to spin frustration while most unfrustrated materials have values $f = 2-5$.[41] From Table S4, $Mn_{1.5}Co_{0.5}P_2S_6$ has the largest $f = 5.2$, while the other samples have $f = 2-3$. This indicates that the frustration in $Mn_xCo_{2-x}P_2S_6$ is relatively low and that there is an overall antiferromagnetic ordering present.

From Figure 5, it also can be seen that there is a distinct dependence on the alloying ratio of Mn:Co and the behavior of the magnetic susceptibility. With the introduction of Co relative to Mn, the Curie−Weiss constant increases until it peaks at $MnCoP_2S_6$ and then decreases once again. A similar behavior in the Curie−Weiss constant has been previously reported by Chandrasekharan et al. who observed a suppression of AFM character in $Mn_xZn_{2-x}P_2S_6$ when a greater concentration of Zn is introduced relative to Mn.[42] Monometallic $Zn_2P_2S_6$ is a nonmagnetic system, so by alloying a greater concentration of Zn into $Mn_xZn_{2-x}P_2S_6$, the long-range antiferromagnetic ordering is diluted.[42] In the case of $Mn_xCo_{2-x}P_2S_6$, both $Mn_2P_2S_6$ and $Co_2P_2S_6$ are antiferromagnetic but of different magnetic anisotropy so when the ratio of Mn/Co approaches 1:1, a greater amount of compensation between Mn and Co will contribute to the dilution of the magnitude of the antiferromagnetic ordering but will require further investigations outside the scope of this paper.

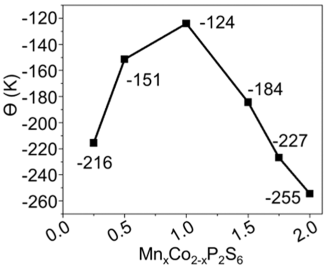

Figure 5. Plot of the Curie−Weiss temperature as a function of composition in $Mn_xCo_{2-x}P_2S_6$. With the addition of a greater concentration of Co relative to Mn, the Curie−Weiss temperature increases until it reaches a maximum when Mn and Co are at parity and then decreases with further addition of Co.

3.5. X-ray Photoelectron (XPS) and Ultraviolet Photoelectron Spectroscopy (UPS). Changes in the composition of Mn and Co in these alloyed systems can potentially alter the electrical properties and charge states of constituent cations. X-ray photoelectron spectroscopy (XPS) is vital to observe these changes at the atomic scale. XPS is conducted under UHV (refer to Methods in Section 2.3) using an Al Kα source. As is the case with our previous study on $Fe_xCo_{2-x}P_2S_6$,[20] the expected charge state of the Mn and Co cations is 2+, which charge balances the $[P_2S_6]^{4-}$ units. Figure 6a shows the XPS spectra for the mix-metal-alloyed compounds and indicates each sample's respective Mn and Co oxidation states. The $2p_{3/2}$ and $2p_{1/2}$ at 640 and 652 eV correspond to the Mn 2p states[43] while 781 and 795 eV correspond to the Co 2p states.[44−46] The states at 640 and 781.1 eV correspond to the Mn^{2+} and Co^{2+} in the octahedral sites.[44,47] Upon introduction of Mn into $Co_2P_2S_6$, an inverse dependence between the intensity of the Mn and Co 2p states is observed, which further confirms the linear trend in the nominal stoichiometry of these alloyed systems. The fitting of the Mn 2p and Co 2p XPS spectra as shown in Figure S12 indicates the presence of shake-up satellite peaks as well as the expected $2p_{3/2}$ and $2p_{1/2}$ peaks. Interestingly, it is observed that there is a doublet splitting in the Mn $2p_{3/2}$ and $2p_{1/2}$ peaks and the Co $2p_{3/2}$ and $2p_{1/2}$ peaks. This doublet splitting in Mn $2p_{3.2}$ has been previously observed in $Mn_2P_2S_6$ by Shifa et al[45] and Wang et al.[46] Wang et al. further observed doublet splitting in Mn $2p_{1/2}$ as well as doublet splitting in Co $2p_{3/2}$ and Co $2p_{1/2}$.[46] The existence of this doublet splitting in both Mn 2p and Co 2p peaks is attributed to oxidation states of Mn^{2+}, Mn^{3+}, Co^{2+}, and Co^{3+}, respectively.[46] The observation of Mn^{3+} and Co^{3+} oxidation states is attributed to surface oxidation that will likely be present after liquid exfoliation and drop-casting. As is previously discussed, the TEM SAED analysis of the alloyed $Mn_xCo_{2-x}P_2S_6$ indicates that all samples analyzed were of the same symmetry as monometallic $Mn_2P_2S_6$ or $Co_2P_2S_6$ when viewed along the out-of-plane direction and will be of similar structure. Therefore, in the bulk, M^{3+} cannot charge balance with the $[P_2S_6]^{4-}$ anion unit, and Mn and Co will be in a 2+ oxidation state.

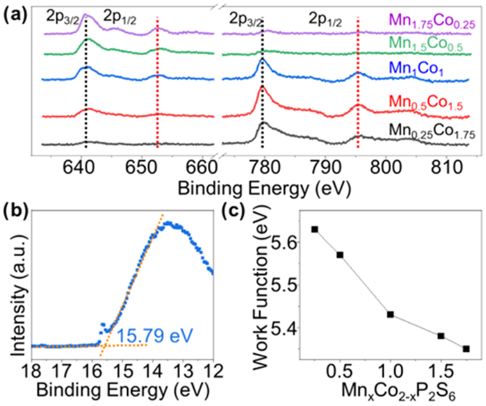

Figure 6. (a) XPS spectra for Mn and Co with $2p_{3/2}$ and $2p_{1/2}$ states indicated. (b) UPS spectra and line fits to determine E_{cutoff} for $MnCoP_2S_6$. (c) Extracted work function difference of the alloyed $Mn_xCo_{2-x}P_2S_6$ systems.

Ultraviolet photoelectron spectroscopy (UPS) is used to further explore the electronic structure of $Mn_xCo_{2-x}P_2S_6$. The UPS spectrum for $MnCoP_2S_6$ is shown in Figure 6b. All UPS spectra are shown in Figure S14. The work function of each bimetallic $Mn_xCo_{2-x}P_2S_6$ system is determined by the equation: $\Phi = h\nu - (E_{\text{cutoff}} - E_F)$.[48] Linear fits to determine the binding energy cutoff (E_{cutoff}) are shown in Figure 6b and Figure S14.[48,49] Figure 6c shows a relation between the derived work function and the concentration of Mn in $Mn_xCo_{2-x}P_2S_6$. A linear reduction in the work function from 5.63 to 5.35 eV is observed as a function of Mn concentration from $Mn_{0.25}Co_{1.75}P_2S_6$ to $Mn_{1.75}Co_{0.5}P_2S_6$. A likely explanation for this distinct shift is due to the difference in electronegativity between Mn and Co.[50] Shifa et al. have previously reported on the work functions of $Mn_2P_2S_6$ and $Mn_2P_2Se_6$ in which they found $Mn_2P_2S_6$ to have a higher work function due to the inherently higher electronegativity of S compared to Se.[45] As Mn has a lower electronegativity, the higher concentration of Mn in $Mn_xCo_{2-x}P_2S_6$ will decrease the overall binding energy and resulting work function.

4.0. Summary and Conclusions. We have conducted a comprehensive structural, electronic, and magnetic analysis of the bimetallic metal thiophosphate, $Mn_xCo_{2-x}P_2S_6$. Bimetallic $Mn_xCo_{2-x}P_2S_6$ is synthesized using our recently developed P_2S_5 flux method to stabilize the Co cation in the alloyed solid solutions. Both elemental and structural analyses confirm a homogeneous distribution of both Mn and Co over the given length scales of several hundreds of nanometers laterally and through multilayer thicknesses. However, it must be noted that some P_xS_y impurity phases were found in a minority of the bulk ingots of synthesized samples ($MnCoP_2S_6$) due to residuals from the P_2S_5 flux even if the majority of product is the alloyed $Mn_xCo_{2-x}P_2S_6$. Phonon mode fingerprints with both intensity and Raman shifts of the four most prominent Raman peaks, 2 A_g and 2 Ag + B_g, are observed. Similar to the previously studied $Fe_xCo_{2-x}P_2S_6$ system, decreasing the Co concentration saw a decrease in the $P^{(4)}(\sim 240\ \text{cm}^{-1})/P^{(5)}(\sim 280\ \text{cm}^{-1})$ ratio and an increase in the $P^{(6)}(\sim 380\ \text{cm}^{-1})/P^{(2)}(\sim 150\ \text{cm}^{-1})$ ratio.

Magnetic susceptibility measurements indicate that all studied alloys of $Mn_xCo_{2-x}P_2S_6$ adopt an antiferromagnetic ordering with a Néel temperature dependent on the alloying ratio of Mn and Co, where $Mn_{1.5}Co_{0.5}P_2S_6$ exhibited the lowest Néel temperature. A broad maximum and associated T_{Max} is observed for nearly all alloyed $Mn_xCo_{2-x}P_2S_6$ except $MnCoP_2S_6$ where this broad maximum is completely suppressed. These broad maxima in the magnetic susceptibility curves are due to local spin ordering. Magnetic frustration is unlikely to occur in the alloyed $Mn_xCo_{2-x}P_2S_6$ as indicated by the small frustration parameter f. A notable increase in the magnetic susceptibility is observed at $T < 30$ K, below the paramagnetic-to-antiferromagnetic transition temperature, $T_{\text{Néel}}$, that is attributed to the minute presence of impurities. It is interesting to note that specifically for $Co_2P_2S_6$ that the presence of higher amounts of $Co(P,S,)_2$ may be apparent that was not detected by either PXRD or Raman, further demonstrating the difficulty in isolating phase-pure $Co_2P_2S_6$. In support of both the Raman and magnetic susceptibility findings, the overall XPS signal intensity of all of the studied alloys of $Mn_xCo_{2-x}P_2S_6$ follows a linear trend in accordance with the nominal stoichiometry of all alloyed systems. The presence of doublet splitting in the Mn and Co $2p_{1/2}$ and $2p_{3/2}$ peaks suggests the presence of mixed states of Mn^{2+}/Mn^{3+} and Co^{2+}/Co^{3+}. Furthermore, the correlation between the alloying ratio of Mn to Co and its work function is established. With an increasing ratio of Mn:Co, the work function of the resulting alloy will decrease, likely due to the lower electronegativity of Mn relative to Co. This work has provided a structural, magnetic, and electronic analysis of the $Mn_xCo_{2-x}P_2S_6$ series and will provide additional insight into engineering chalcophosphates for specific applications. We also hope that this work will stimulate other further studies into layered magnetic structures and alloyed chalcophosphate systems.

■ ASSOCIATED CONTENT

Supporting Information

The Supporting Information is available free of charge at https://pubs.acs.org/doi/10.1021/acs.inorgchem.2c01116.

> Experimental methods and physical property measurements; table of precursor amounts for synthesis of $Mn_xCo_{2-x}P_2S_6$ (x = 0.25, 0.5, 1.0, 1.5, 1.75); supplementary HRTEM and diffraction patterns (experimental and simulated) for $Mn_{0.25}Co_{1.75}P_2S_6$ and $Mn_{1.75}Co_{0.25}P_2S_6$; supplementary STEM-EDS maps and spectra for $Mn_xCo_{2-x}P_2S_6$ (x = 0.25, 1.0, 1.5, 1.75); simulated Raman modes; ZFC and FC curves of magnetic susceptibility plots for $Mn_xCo_{2-x}P_2S_6$; inverse magnetic susceptibility plots for $Mn_xCo_{2-x}P_2S_6$ (x = 0.25, 0.5, 1.0, 1.5, 1.75); table of Néel temperature, magnetic moments μ_{eff}, and Curie–Weiss temperature Θ; M vs H for $MnCoP_2S_6$; XPS Mn, Co, P, and S spectra for $Mn_xCo_{2-x}P_2S_6$ (x = 0.25, 0.5, 1.0, 1.5, 1.75); and UPS spectra for $Mn_xCo_{2-x}P_2S_6$ (x = 0.25, 0.5, 1.0, 1.5, 1.75) (PDF)

■ AUTHOR INFORMATION

Corresponding Authors

Mercouri G. Kanatzidis − *Department of Chemistry, Northwestern University, Evanston, Illinois 60208, United States;* orcid.org/0000-0003-2037-4168; Email: m-kanatzidis@northwestern.edu

Vinayak P. Dravid − *Department of Material Science and Engineering, Northwestern University, Evanston, Illinois 60208, United States; Northwestern University Atomic and Nanoscale Characterization Experimental (NUANCE) Center and International Institute for Nanotechnology (IIN), Northwestern University, Evanston, Illinois 60208, United States;* orcid.org/0000-0002-6007-3063; Email: v-dravid@northwestern.edu

Authors

Matthew Cheng − *Department of Material Science and Engineering, Northwestern University, Evanston, Illinois 60208, United States;* orcid.org/0000-0002-1062-5974

Abishek K. Iyer − *Department of Chemistry, Northwestern University, Evanston, Illinois 60208, United States;* orcid.org/0000-0002-8582-3895

Xiuquan Zhou − *Materials Science Division, Argonne National Laboratory, Lemont, Illinois 60439, United States*

Alexander Tyner − *Graduate program in Applied Physics, Northwestern University, Evanston, Illinois 60208, United States*

Yukun Liu − *Department of Material Science and Engineering, Northwestern University, Evanston, Illinois 60208, United States*

M. Arslan Shehzad − *Department of Material Science and Engineering, Northwestern University, Evanston, Illinois 60208, United States; Northwestern University Atomic and Nanoscale Characterization Experimental (NUANCE)*

Center, Northwestern University, Evanston, Illinois 60208, United States; orcid.org/0000-0002-6260-5764

Pallab Goswami − *Graduate program in Applied Physics and Department of Physics and Astronomy, Northwestern University, Evanston, Illinois 60208, United States*

Duck Young Chung − *Materials Science Division, Argonne National Laboratory, Lemont, Illinois 60439, United States*

Complete contact information is available at:
https://pubs.acs.org/10.1021/acs.inorgchem.2c01116

Author Contributions

○M.C. and A.K. contributed equally to this work.

Notes

The authors declare no competing financial interest.

■ ACKNOWLEDGMENTS

This work was supported by NSF Division of Material Research (NSF Grant DMR-1929356 - Program Manager: Lynnette Madsen). This work made use of the EPIC facility of Northwestern University's NUANCE Center, which has received support from the SHyNE Resource [National Science Foundation (NSF) Grant ECCS-2025633], Northwestern's MRSEC program (NSF Grant DMR-1720139), the Keck Foundation, and the State of Illinois through IIN. The materials synthesis in this work was partially supported by the Army Research Office (Grant W911NF1910335). M.C. acknowledges support from the NSF Graduate Research Fellowship under Grant DGE-1842165. A.T. and P.G. are supported by the National Science Foundation MRSEC program (DMR-1720319) at the Materials Research Center of Northwestern University, and the start-up funds of P. G. provided by Northwestern University. Work at Argonne National Laboratory (magnetic susceptibility measurements) was supported by the U.S. Department of Energy, Office of Science, Basic Energy Sciences, Materials Science and Engineering Division. The authors thank Eric Qian from the Kanatzidis Research Group at Northwestern University and Yea-Shine Lee from the Dravid group at Northwestern University for intellectual contributions to this work.

■ REFERENCES

(1) Wang, F.; Shifa, T. A.; Yu, P.; He, P.; Liu, Y.; Wang, F.; Wang, Z.; Zhan, X.; Lou, X.; Xia, F.; He, J. New Frontiers on van Der Waals Layered Metal Phosphorous Trichalcogenides. *Adv. Funct. Mater.* **2018**, *28*, No. 1802151.

(2) Ouvrard, G.; Brec, R.; Rouxel, J. Structural Determination of Some MPS3 Layered Phases (M = Mn, Fe, Co, Ni and Cd. *Mater. Res. Bull.* **1985**, *20*, 1181−1189.

(3) He, Y.; Dai, Y.-D.; Huang, H.; Lin, J.; Hsia, Y. The Ordering Distribution of the Metal Ions in the Layered Cation-Mixed Phosphorus Trisulfides MnxFe1−xPS3. *J. Alloys Compd.* **2003**, *359*, 41−45.

(4) Chica, D. G.; He, Y.; McCall, K. M.; Chung, D. Y.; Pak, R. O.; Trimarchi, G.; Liu, Z.; De Lurgio, P. M.; Wessels, B. W.; Kanatzidis, M. G. Publisher Correction: Direct Thermal Neutron Detection by the 2D Semiconductor 6LiInP2Se6. *Nature* **2020**, *579*, E9.

(5) Du, K.-z.; Wang, X.; Liu, Y.; Hu, P.; Utama, M. I. B.; Gan, C. K.; Xiong, Q.; Kloc, C. Weak Van Der Waals Stacking, Wide-Range Band Gap, and Raman Study on Ultrathin Layers of Metal Phosphorus Trichalcogenides. *ACS Nano* **2016**, *10*, 1738−1743.

(6) Fujii, Y.; Kobayashi, M.; Miura, A.; Rosero-Navarro, N. C.; Li, M.; Sun, J.; Kotobuki, M.; Lu, L.; Tadanaga, K. Fe−P−S Electrodes for All-Solid-State Lithium Secondary Batteries Using Sulfide-Based Solid Electrolytes. *J. Power Sources* **2020**, *449*, No. 227576.

(7) Si, M.; Liao, P.-Y.; Qiu, G.; Duan, Y.; Ye, P. D. Ferroelectric Field-Effect Transistors Based on MoS_2 and $CuInP_2S_6$ Two-Dimensional van Der Waals Heterostructure. *ACS Nano* **2018**, *12*, 6700−6705.

(8) Xie, Q.-Y.; Wu, M.; Chen, L.-M.; Bai, G.; Zou, W.-Q.; Wang, W.; He, L. Crystallographic and Magnetic Properties of van Der Waals Layered FePS3 Crystal\ast. *Chin. Phys. B* **2019**, *28*, No. 056102.

(9) Toyoshima, W.; Masubuchi, T.; Watanabe, T.; Takase, K.; Matsubayashi, K.; Uwatoko, Y.; Takano, Y. Pressure Dependence of the Magnetic Properties of MnPS3. *J. Phys. Conf. Ser.* **2009**, *150*, No. 042215.

(10) Wildes, A. R.; Simonet, V.; Ressouche, E.; Ballou, R.; McIntyre, G. J. The Magnetic Properties and Structure of the Quasi-Two-Dimensional Antiferromagnet CoPS3. *J. Phys.: Condens. Matter* **2017**, *29*, No. 455801.

(11) Wildes, A. R.; Simonet, V.; Ressouche, E.; McIntyre, G. J.; Avdeev, M.; Suard, E.; Kimber, S. A. J.; Lançon, D.; Pepe, G.; Moubaraki, B.; Hicks, T. J. Magnetic Structure of the Quasi-Two-Dimensional Antiferromagnet $NiPS_3$. *Phys. Rev. B* **2015**, *92*, No. 224408.

(12) Joy, P. A.; Vasudevan, S. Magnetism in the Layered Transition-Metal Thiophosphates MPS_3 (M =Mn, Fe, and Ni). *Phys. Rev. B* **1992**, *46*, 5425−5433.

(13) Rao, R. R.; Raychaudhuri, A. K. Magnetic Studies of a Mixed Antiferromagnetic System Fe1−xNixPS3. *J. Phys. Chem. Solids* **1992**, *53*, 577−583.

(14) Ressouche, E.; Loire, M.; Simonet, V.; Ballou, R.; Stunault, A.; Wildes, A. Magnetoelectric $MnPS_3$ as a Candidate for Ferrotoroidicity. *Phys. Rev. B* **2010**, *82*, No. 100408.

(15) Masubuchi, T.; Hoya, H.; Watanabe, T.; Takahashi, Y.; Ban, S.; Ohkubo, N.; Takase, K.; Takano, Y. Phase Diagram, Magnetic Properties and Specific Heat of Mn1−xFexPS3. *J. Alloys Compd.* **2008**, *460*, 668−674.

(16) Shemerliuk, Y.; Zhou, Y.; Yang, Z.; Cao, G.; Wolter, A. U. B.; Büchner, B.; Aswartham, S. Tuning Magnetic and Transport Properties in Quasi-2D (Mn1−xNix)2P2S6 Single Crystals. *Electron. Mater.* **2021**, *2*, 284−298.

(17) Goossens, D. J.; Brazier-Hollins, S.; James, D. R.; Hutchison, W. D.; Hester, J. R. Magnetic Structure and Glassiness In. *J. Magn. Magn. Mater.* **2013**, *334*, 82−86.

(18) Xiao-Bing, Y.; Xingguo, C.; Jingui, Q. Synthesis and Magnetic Properties of New Layered $Ni_xMn_{1-x}PS_3$ and Their Intercalation Compounds. *Acta Chim. Sin.* **2011**, *69*, 1017.

(19) Chica, D. G.; Iyer, A. K.; Cheng, M.; Ryan, K. M.; Krantz, P.; Laing, C.; dos Reis, R.; Chandrasekhar, V.; Dravid, V. P.; Kanatzidis, M. G. P_2S_5 Reactive Flux Method for the Rapid Synthesis of Mono- and Bimetallic 2D Thiophosphates $M_{2-x}M'_xP_2S_6$. *Inorg. Chem.* **2021**, *60*, 3502−3513.

(20) Cheng, M.; Lee, Y.-S.; Iyer, A. K.; Chica, D. G.; Qian, E. K.; Shehzad, M. A.; dos Reis, R.; Kanatzidis, M. G.; Dravid, V. P. Mixed Metal Thiophosphate $Fe_{2-x}Co_xP_2S_6$: Role of Structural Evolution and Anisotropy. *Inorg. Chem.* **2021**, *60*, 17268−17275.

(21) Kresse, G.; Furthmüller, J. Efficient Iterative Schemes for *Ab Initio* Total-Energy Calculations Using a Plane-Wave Basis Set. *Phys. Rev. B* **1996**, *54*, 11169−11186.

(22) Giannozzi, P.; Baseggio, O.; Bonfà, P.; Brunato, D.; Car, R.; Carnimeo, I.; Cavazzoni, C.; de Gironcoli, S.; Delugas, P.; Ferrari Ruffino, F.; Ferretti, A.; Marzari, N.; Timrov, I.; Urru, A.; Baroni, S. Q uantum ESPRESSO toward the Exascale. *J. Chem. Phys.* **2020**, *152*, No. 154105.

(23) Perdew, J. P.; Zunger, A. Self-Interaction Correction to Density-Functional Approximations for Many-Electron Systems. *Phys. Rev. B* **1981**, *23*, 5048−5079.

(24) Grimme, S. Semiempirical GGA-Type Density Functional Constructed with a Long-Range Dispersion Correction. *J. Comput. Chem.* **2006**, *27*, 1787−1799.

(25) Ouvrard, G.; Brec, R.; Rouxel, J. Structural Determination of Some MPS3 Layered Phases (M = Mn, Fe, Co, Ni and Cd). *Mater. Res. Bull.* **1985**, *20*, 1181−1189.

(26) Susner, M. A.; Chyasnavichyus, M.; McGuire, M. A.; Ganesh, P.; Maksymovych, P. Metal Thio- and Selenophosphates as Multifunctional van Der Waals Layered Materials. *Adv. Mater.* **2017**, *29*, No. 1602852.

(27) Murayama, C.; Okabe, M.; Urushihara, D.; Asaka, T.; Fukuda, K.; Isobe, M.; Yamamoto, K.; Matsushita, Y. Crystallographic Features Related to a van Der Waals Coupling in the Layered Chalcogenide FePS$_3$. *J. Appl. Phys.* **2016**, *120*, No. 142114.

(28) *Generated Using SingleCrystalTM: A Single-Crystal Diffraction Program for Mac and Windows*; CrystalMaker Software Ltd: Oxford, England, Www.Crystalmaker.Com.

(29) Kargar, F.; Coleman, E. A.; Ghosh, S.; Lee, J.; Gomez, M. J.; Liu, Y.; Magana, A. S.; Barani, Z.; Mohammadzadeh, A.; Debnath, B.; Wilson, R. B.; Lake, R. K.; Balandin, A. A. Phonon and Thermal Properties of Quasi-Two-Dimensional FePS$_3$ and MnPS$_3$ Antiferromagnetic Semiconductors. *ACS Nano* **2020**, *14*, 2424−2435.

(30) Sun, Y.-J.; Tan, Q.-H.; Liu, X.-L.; Gao, Y.-F.; Zhang, J. Probing the Magnetic Ordering of Antiferromagnetic MnPS$_3$ by Raman Spectroscopy. *J. Phys. Chem. Lett.* **2019**, *10*, 3087−3093.

(31) Kim, K.; Lim, S. Y.; Kim, J.; Lee, J.-U.; Lee, S.; Kim, P.; Park, K.; Son, S.; Park, C.-H.; Park, J.-G.; Cheong, H. Antiferromagnetic Ordering in van Der Waals 2D Magnetic Material MnPS$_3$ Probed by Raman Spectroscopy. *2D Mater.* **2019**, *6*, No. 041001.

(32) Liu, Q.; Wang, L.; Fu, Y.; Zhang, X.; Huang, L.; Su, H.; Lin, J.; Chen, X.; Yu, D.; Cui, X.; Mei, J.-W.; Dai, J.-F. Magnetic Order in XY-Type Antiferromagnetic Monolayer CoPS 3 Revealed by Raman Spectroscopy. *Phys. Rev. B* **2021**, *103*, No. 235411.

(33) Xu, H.; Wang, S.; Ouyang, J.; He, X.; Chen, H.; Li, Y.; Liu, Y.; Chen, R.; Yang, J. Surface Modification of Multilayer FePS3 by Ga Ion Irradiation. *Sci. Rep.* **2019**, *9*, No. 15219.

(34) Mayorga-Martinez, C. C.; Sofer, Z.; Sedmidubský, D.; Huber, Š.; Eng, A. Y. S.; Pumera, M. Layered Metal Thiophosphite Materials: Magnetic, Electrochemical, and Electronic Properties. *ACS Appl. Mater. Interfaces* **2017**, *9*, 12563−12573.

(35) Hashemi, A.; Komsa, H.-P.; Puska, M.; Krasheninnikov, A. V. Vibrational Properties of Metal Phosphorus Trichalcogenides from First-Principles Calculations. *J. Phys. Chem. C* **2017**, *121*, 27207−27217.

(36) Bernasconi, M.; Marra, G. L.; Benedek, G.; Miglio, L.; Jouanne, M.; Julien, C.; Scagliotti, M.; Balkanski, M. Lattice Dynamics of Layered MP X 3 (*M*= Mn,Fe,Ni,Zn; *X*= S,Se) Compounds. *Phys. Rev. B* **1988**, *38*, 12089−12099.

(37) Chen, Y.; Dumcenco, D. O.; Zhu, Y.; Zhang, X.; Mao, N.; Feng, Q.; Zhang, M.; Zhang, J.; Tan, P.-H.; Huang, Y.-S.; Xie, L. Composition-Dependent Raman Modes of Mo$_{1-x}$W$_x$S$_2$ Monolayer Alloys. *Nanoscale* **2014**, *6*, 2833−2839.

(38) Dumcenco, D. O.; Su, Y.-C.; Wang, Y.-P.; Chen, K.-Y.; Huang, Y.-S.; Ho, C.-H.; Tiong, K.-K. Polarization Dependent Raman Active Modes Study of the Mo 1-x W x S2 Mixed Layered Crystals. *Chin. J. Phys.* **2011**, *49*, 270−277.

(39) Bai, W.; Hu, Z.; Xiao, C.; Guo, J.; Li, Z.; Zou, Y.; Liu, X.; Zhao, J.; Tong, W.; Yan, W.; Qu, Z.; Ye, B.; Xie, Y. Parasitic Ferromagnetism in Few-Layered Transition-Metal Chalcogenophosphate. *J. Am. Chem. Soc.* **2020**, *142*, 10849−10855.

(40) Nahigian, H.; Steger, J.; Arnott, R. J.; Wold, A. Preparation and Properties of the System CoPxS2−x. *J. Phys. Chem. Solids* **1974**, *35*, 1349−1354.

(41) Balents, L. Spin Liquids in Frustrated Magnets. *Nature* **2010**, *464*, 199−208.

(42) Chandrasekharan, N.; Vasudevan, S. Dilution of a Layered Antiferromagnet: Magnetism in Mn x Zn 1 − x P S 3. *Phys. Rev. B* **1996**, *54*, 14903−14906.

(43) Ilton, E. S.; Post, J. E.; Heaney, P. J.; Ling, F. T.; Kerisit, S. N. XPS Determination of Mn Oxidation States in Mn (Hydr)Oxides. *Appl. Surf. Sci.* **2016**, *366*, 475−485.

(44) Oku, M.; Hirokawa, K. X-Ray Photoelectron Spectroscopy of Co3O4, Fe3O4, Mn3O4, and Related Compounds. *J. Electron Spectrosc. Relat. Phenom.* **1976**, *8*, 475−481.

(45) Shifa, T. A.; Wang, F.; Cheng, Z.; He, P.; Liu, Y.; Jiang, C.; Wang, Z.; He, J. High Crystal Quality 2D Manganese Phosphorus Trichalcogenide Nanosheets and Their Photocatalytic Activity. *Adv. Funct. Mater.* **2018**, *28*, No. 1800548.

(46) Wang, R.; Huang, J.; Zhang, X.; Han, J.; Zhang, Z.; Gao, T.; Xu, L.; Liu, S.; Xu, P.; Song, B. Two-Dimensional High-Entropy Metal Phosphorus Trichalcogenides for Enhanced Hydrogen Evolution Reaction. *ACS Nano* **2022**, *16*, 3593.

(47) Menezes, P. W.; Indra, A.; Gutkin, V.; Driess, M. Boosting Electrochemical Water Oxidation through Replacement of O$_h$ Co Sites in Cobalt Oxide Spinel with Manganese. *Chem. Commun.* **2017**, *53*, 8018−8021.

(48) Kim, J. W.; Kim, A. Absolute Work Function Measurement by Using Photoelectron Spectroscopy. *Curr. Appl. Phys.* **2021**, *31*, 52−59.

(49) Schultz, T.; Lenz, T.; Kotadiya, N.; Heimel, G.; Glasser, G.; Berger, R.; Blom, P. W. M.; Amsalem, P.; de Leeuw, D. M.; Koch, N. Reliable Work Function Determination of Multicomponent Surfaces and Interfaces: The Role of Electrostatic Potentials in Ultraviolet Photoelectron Spectroscopy. *Adv. Mater. Interfaces* **2017**, *4*, No. 1700324.

(50) Li, K.; Xue, D. Estimation of Electronegativity Values of Elements in Different Valence States. *J. Phys. Chem. A* **2006**, *110*, 11332−11337.